JOURNAL OF MATERIALS SCIENCE 27 (1992) 2437–2443

Effect of laser surface melted zirconium alloys on microstructure and corrosion resistance

W. REITZ
Babcock and Wilcox, c/o ICF Kaiser Engineering, 1800 Harrison street, Oakland, CA 94612, USA

J. RAWERS
US Bureau of Mines, 1450 Queen street, Albany, OR 97321, USA

Zirconium alloys were laser surface melted (LSM) using a continuous wave CO_2 laser at energy densities of 4,7 and 10 kJ cm^{-2}. LSM samples examined using SEM and optical microscopy exhibited resolidified regions with several different microstructures, including ultrafine martensite. Corrosion performance was obtained by steam autoclave tests and immersion tests in 10% $FeCl_3$ at room temperature. Coarser microstructures performed better than fine microstructures in autoclave tests, while fine microstructures performed better than coarse microstructures in 10% $FeCl_3$ immersion tests. Accelerated corrosion in the autoclave and immersion tests was observed to occur near the laser beam overlap region. The surface chemistry was examined for alloy segregation using secondary iron mass spectroscopy. Tin and iron alloy elements segregated near the periphery of each melt pool. Segregated regions containing increased iron concentrations associated with each laser pass were responsible for accelerated corrosion.

1. Introduction

With the advent of nuclear power in the fifties, it was found that zirconium possesses several properties which made it desirable for use in nuclear reactors [1–3]. These properties include high corrosion resistance, good mechanical properties, and low thermal neutron absorption cross-section [4].

For example, when zirconium alloys are exposed to high-temperature steam, the alloys quickly form a very hard and strongly adherent oxide film that protects the material from further rapid oxidation [1, 3–7]. In addition to the oxidation resistance in a wide range of chemical environments, zirconium is more corrosion resistant than stainless steel. In most environments, zirconium's resistance is the result of a thin self-generating oxide film on the metal that makes it appear more noble than the electromotive series indicates for pure zirconium. However, it is not resistant to fluoride, chlorine, concentrated sulphuric acid, or ferric and cupric chlorides [8–12].

Metastable structure synthesis by laser melting and rapid quenching has opened an exciting era in physical metallurgy [13]. Rapid quenching provides the means for tailoring certain properties (microstructure, alloy composition, and metastable phases), previously unattainable, to meet specific material requirements [14–16]. Improvement of surface sensitive properties such as corrosion protection, microhardness, and wear resistance have been achieved by laser processing at high quenching rates [14, 15, 17, 18].

In the laser surface melting (LSM) process, the absorbed energy is instantaneously transferred to the lattice. The near surface regions rapidly attain the melting temperature. When the laser beam is removed, the subsurface metal rapidly quenches the liquid metal. Interdiffusion in the melt continues. However, solidification of the metal behind the liquid/solid interface occurs so rapidly that solid state diffusion may be neglected [19, 20].

Metallurgically, laser-processed material has three different metallographical regions (zones): the melt zone, the heat-affected zone adjacent to the melt zone, and the unaffected base metal. The heat-affected zone (HAZ) is a function of laser processing [21–24]. Specifically, the HAZ size is directly related to laser power and specimen thickness, thermal conductivity, heat capacity, etc. Additionally, the HAZ size is inversely related to laser beam speed [25, 26].

Studies [27–29] have shown that composition gradients exist within the molten pool from the edge to the centre or from the bottom to the top, due to solidification initiating at the edge and/or at the bottom of the molten pool.

In a recent study [30] the microstructure, chemical homogeneity, and lattice parameters of LSM Zr–4 were examined. Martensitic transformation occurred without the development of any second phase.

LSM offers several unique opportunities for metal processing. This project investigated the corrosion properties of LSM zirconium-based alloys and examined the processed material to determine the mechanism responsible for corrosion. The data indicate

0022–2461

TABLE I Zirconium alloy fabrication conditions and composition for ingots A–I

		Pure Zr		Zr-702		Zr-4		
		A	B	D	E	G	H	I
Thickness (mm)		3.4	3.4	2.0	3.4	3.4	3.4	3.4
Fabrication		cold	hot	cold	cold	cold	cold	cold
Element (p.p.m.)	Sn	500	500	1900	100	14,800	15,800	14,700
	Fe	600	600	850	600	2080	2100	2050
	Cr	50	50	120	70	1080	1160	1100
	Fe/Cr	12	12	7.1	8.5	2.0	1.9	1.9
	O	800	800	1500	1000	1240	1520	1350
	N	30	30	48	65	32	20	28
	C	100	100	170	140	160	160	140
	HF	73	73	1000	100	77	43	42
	Al	63	63	100	90	65	41	60
	Si	25	25	68	42	96	100	83

that microstructure and chemical microsegregation are the controlling factors for corrosion performance of LSM material.

2. Experimental procedure

The three zirconium alloys used (Teledyne Wah Chang, Albany) were pure zirconium, Zr-702, and Zr-4. The compositions and fabrication histories of these alloys are given in Table I.

Zirconium is well known for its ability to getter oxygen and the tenacity of the oxide. During typical fabrication processes an oxide layer forms as a result of hot working in the atmosphere. This oxide film was removed from the wrought product prior to laser processing by metallographically polishing using 600 grit SiO_2 and then rinsing in tap water and alcohol.

Laser processing was performed with an AVCO HLP-1 laser (CO_2 continuous wave laser capable of 7 kW power) at the Materials Engineering Research Laboratory (MERL), University of Illinois. Two different sample geometries were laser processed: 4 in × 20 in (~ 10 cm × 50 cm) plates for immersion testing and $1\frac{1}{4}$ in × $1\frac{3}{4}$ in (~ 3.2 cm × 4.4 cm) for autoclave testing.

Material to be LSM was placed on a computer-controlled table capable of x–y–z motion. The laser beam was stationary and the table moved beneath the beam. After each pass the table was indexed one-half the beam width to provide 50% overlap and ensure complete coverage. Beam width was adjustable by using mirrors within the laser unit and was measured from the width of a resolidified molten line on the material surface. All laser processing was conducted in the same direction. After each laser pass the table was repositioned to the start line and then indexed. The laser processing was conducted in an open atmospheric environment with a helium cover gas over the molten area. The laser processing parameters used in this study are presented in Table II.

Control coupons with three different surface conditions (non-LSM) were prepared: (1) as-rolled, (2) as-rolled and grit-blasted, and (3) as-rolled and metallographically polished.

TABLE II Laser processing parameters

Power (kW)	Feed rate (mm s^{-1})	Beam diameter[a] (mm)	Energy density (kJ cm^{-2})	Power density (kW cm^{-2})
3	84	1	4	71
7	42	3	7	99
5	21	3	10	384

[a] Laser beam was focused at the mid-plane of metal thickness.

Immersion coupons were machined from plate stock that had been LSM on only one side. The non-LSM surfaces of the immersion coupons were coated with a protective organic film (Plasti-Dip, PDI Inc.). Two coats were applied to ensure complete protection. This organic material was chosen because it was shown to be non-reacting in the test environment.

Autoclave coupons were machined, grit-blasted, and pickled prior to LSM. (The pickle solution consisted of 3% HF, 35% HNO_3, and 62% H_2O.) The nominal coupon size was $t \times 1.25$ in × 1.75 in (t × 3.2 cm × 4.4 cm). A minimum of 0.01 in. (~ 0.03 cm) was machined from all major surfaces, which is the standard technique to ensure that there will be no oxide contamination in the tested material. Autoclave coupons required 100% LSM processing. After laser processing one face, the coupons were turned over and the backside was laser processed. The coupon sides, which include the hanger hole and four edges, were LSM by allowing the laser beam to run-over the edge, resulting in a melted edge.

Prior to testing, the coupons were weighed (± 0.1 mg) and their dimensions measured (± 0.08 mm). Autoclave coupons were tested in a closed-loop autoclave for seven consecutive 14 day intervals. Each interval operated at 400 ± 5 °C (750 °F) and 10.34 ± 0.6 MPa (1500 p.s.i.g.) steam. In the autoclave, the coupons were hung on a type 300 stainless steel fixture that permitted total surface exposure to the steam environment. Between each test interval, the coupons were removed, air-dried, and visually examined at × 5 to determine the condition of the developing oxide film. The coupons (weighing approximately 2 g each) were weighed to determine the weight gain.

After each weighing and inspection the coupons were returned to the autoclave. The normal weight gain for Zr-4 has been established by industry at less than 35 mg dm^{-2} for the first two-week interval [10].

Immersion tests were performed in a 10% $FeCl_3$ static solution, at room temperature for a total of 34 days (800 h). Coupons were placed in a solution open to the atmosphere. The tray containing the solution and coupons was covered to minimize the normal evaporation that occurs at room temperature. Prior to immersion testing, the coupons were weighed and their dimensions were measured. After applying the protective coating the coupons were reweighed. As part of the test the coupons were removed from the acid solution, rinsed in two water baths and one alcohol bath, and then allowed to air dry. The drying time was 1–2 h. The coupons were weighed every 3–4 days and then replaced in a fresh batch of 10% $FeCl_3$.

Several microscopic techniques were used: optical microscopy, scanning electron microscopy (SEM), SEM microprobe, and secondary ion mass spectrometry (SIMS).

3. Results

3.1 Autoclave

Steam autoclave data are presented in Fig. 1. Oxide formation as measured by weight gain per unit area, is plotted against time. The slope of the curve is the corrosion rate. For this test, two different heats of Zr-4 were employed with two different levels of laser processing (low and medium energy density). The control coupons were as-received wrought material from the same heats as the LSM material, but with a machined surface.

LSM increases the corrosion rate. LSM with the low laser energy density (4 kJ cm^{-2}) produces a corrosion rate that is triple that of the wrought product. LSM with the medium laser energy density (7 kJ cm^{-2}) yields approximately double the corrosion rate of the control.

Autoclave corrosion curves of zirconium alloys typically consist of a cubic pre-transition region, a transition point, and a linear post-transition region [31]. The control samples exhibited the transition point (change from cubic to linear corrosion rate behaviour) at about 35 days (40 mg dm^{-2}) [32] (Table III). The transition point indicates the time at which the protective corrosion film is breached [31]. During the initial corrosion phase in the cubic region, a tightly adherent, protective, corrosion film forms. When cracks develop in the corrosion film, the corrosion rate changes and becomes linear. As the applied laser energy density is reduced, the occurrence of the transition point is delayed (Table III). In the limiting case, the "zero" laser energy density processing is predicted to possess a transition point beyond 55 days and 150 mg dm^{-2}.

Nodule formation was observed after the first two-week autoclave corrosion run (Fig. 3). Subsequent runs did not initiate new nodules, rather the initial nodules appeared to grow, covering more area as exposure time increased, and eventually resulted in coalescence. The nodules were observed to initiate at the edge of the laser overlap regions. The centres of the melt regions were essentially free of nodule formation.

3.2. Immersion

Corrosion rates were determined as weight loss per unit time; as measured by mils per year (m.p.y). There were five different starting zirconium ingots each with three laser processing parameters (Table IV).

TABLE III Transition points[a] and 98 day corrosion rates

	Energy density (kJ cm^{-2})[b]		
	7	4	0[c]
Transition point (days)	42	55	35
transition point (mg dm^{-2})	110	150	40
Corrosion rate after 98 days (mg dm^{-2})	190	250	70

[a] Obtained from Fig. 2.
[b] LSM at 10 kJ cm^{-2} not autoclave tested.
[c] 0 designates "control", non-LSM.

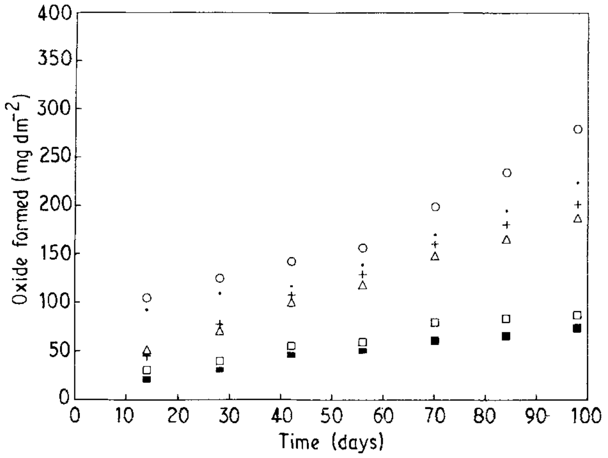

Figure 1 Steam autoclave corrosion rates (98 days). (○) 4/226220, (·) 4/218208, (Δ) 7/226220, (+) 7/218208, (□) zero/226220, (■) zero/218208.

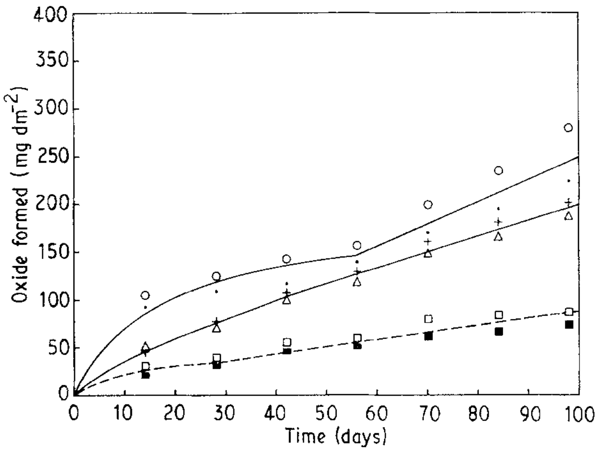

Figure 2 Autoclave transition points. (○) 4/226220, (·) 4/218208, (Δ) 7/226220, (+) 7/218208, (□) zero/226220, (■) zero/218208.

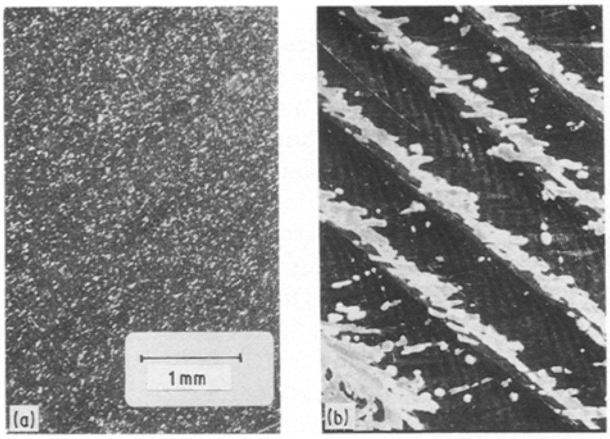

Figure 3 Nodule formation after two weeks in autoclave: (a) control (non- LSM) and (b) 7 kJ cm^{-2}.

TABLE IV Immersion corrosion rates (m.p.y.) summary in table of means[a]

	LSM (kJ cm^{-2})			
Material	10	7	4	Average
A	0.4	0.5	0.2	0.4
B	0.9	0.4	0.3	0.5
G	0.6	0.5	0.4	0.5
D	0.8	0.4	0.2	0.5
E	0.4	0.3	0.2	0.3
Average	0.6	0.4	0.3	0.4

[a] Each value is the average of eight coupons, standard deviation of 0.13.

The corrosion resistance of zirconium is known to be strongly influenced by the condition of the coupon's surface [7, 33]. The grit-blasted surface in 10% $FeCl_3$ yields a poor corrosion resistance of 300 m.p.y. The as-rolled surface exhibits a corrosion rate of 20 m.p.y., whereas a polished surface produces a corrosion rate of 5 m.p.y.

The lowest laser energy density deposition (4 kJ cm^{-2}) resulted in the greatest improvement to corrosion resistance. As the amount of energy applied increased, the corrosion rate was reduced, but still remained an order of magnitude below the polished surface performance and was three orders of magnitude below the grit-blasted surface performance.

After immersion testing, samples were examined under an optical microscope to evaluate types and extent of corrosion. In addition to general surface corrosion, pitting was observed. Pits were evaluated and pit depth determined microscopically by using the fine focus and estimating the depth by the change in focal point. Tendency towards pitting is directly related to the applied laser energy density and to the resulting microstructure, and possibly to the chemical segregation as shown in Fig. 4.

Two corrosion responses, general and pitting, can be seperated by calculating weight loss due to pitting compared to weight loss due to general corrosion. Pit diameter, as determined by optical microscopy, is typically one-half the depth. Using pit depth and diameter, volume (and weight) of the material removed by pitting can be calculated. Table V lists weight of material removed based on volume of pits per total exposed surface area. Based on these data,

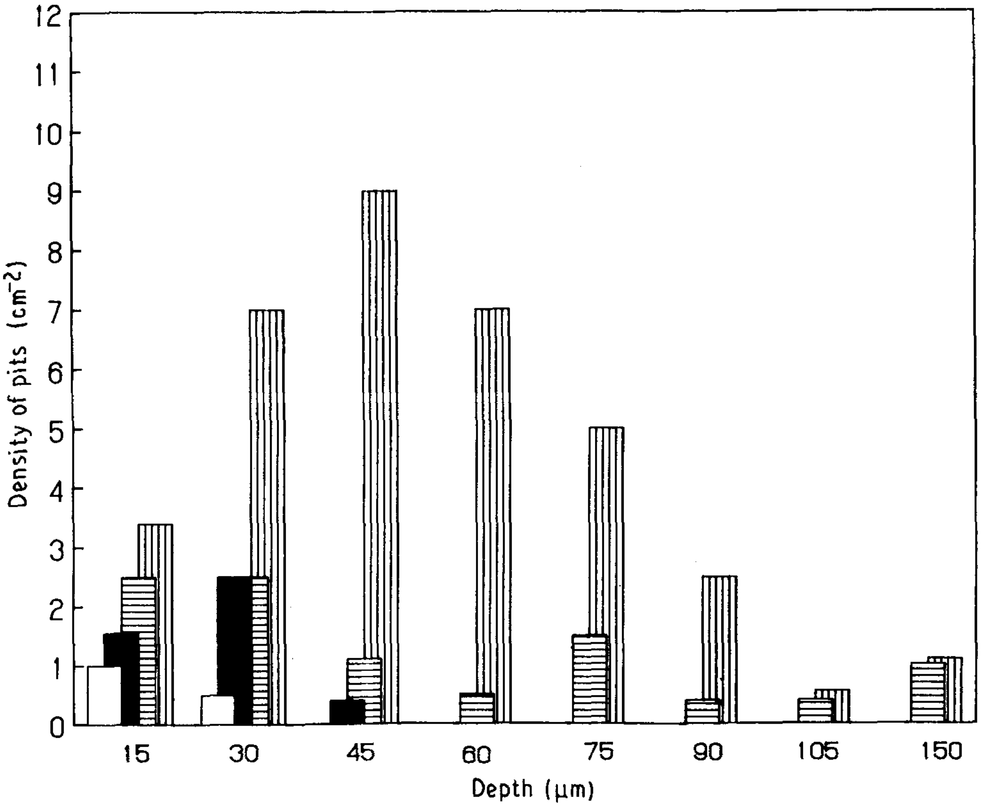

Figure 4 Pitting behaviour. (□) 4 kJ cm^{-2}, (■) 7 kJ cm^{-2}, (▤) 10 kJ cm^{-2}, (▥) controls. (grit blasted).

pitting is responsible for an average of 30% of the corrosion rate as a result of processing with the highest laser energy density (10 kJ cm^{-2}), approximately 2% of the corrosion rate for the medium laser energy density (7 kJ cm^{-2}), and approximately 0.6% of the corrosion rate for the lowest laser energy density (4 kJ cm^{-2}).

The lowest laser energy density (4 kJ cm^{-2}) developed the fewest number of pits and pits with the least depth of penetration. On increasing the laser energy density from 4 to 10 kJ cm^{-2}, the corrosion rate increases from 0.3 to 0.6 m.p.y. (Table IV and Fig. 4). Coincidentally, the propensity towards pitting increases approximately by two orders of magnitude. Pitting behaviour is almost negligible when LSM is at the lowest laser energy density (4 kJ cm^{-2}). The pitting component compared to the overall corrosion represents only a small contribution to the overall corrosion.

3.3 Microstructure and phases

Optical microscopy of laser-processed samples revealed a variety of microstructures. Fig. 5 shows the typical transverse microstructure of starting materials at three different laser processing conditions.

Low-energy densities generate a martensitic type structure that is characterized by an extremely fine lenticular precipitation formation. Martensitic structures typically result from extremely fast quenching from the melt temperature through the beta-phase. Shallow melt-pool depths provide an excellent heat sink via the underlying substrate. Heat transfer occurs in the through-thickness direction as well as laterally.

TABLE V Corrosion rate (m.p.y.) based on pit volume and percentage of total corrosion rate due to pitting

	LSM (kJ cm^{-2})					
	10		7		4	
Material	m.p.y.	%	m.p.y.	%	m.p.y.	%
A	0.3	75	0.01	2	0	0
B	0.06	7	0.01	2	0	0
G	0.24	40	0.01	1	0	0
D	0.30	40	0.01	1	0.03	2
E	0.01	2	0.01	3	0.01	0.5
Average		30		2		0.6

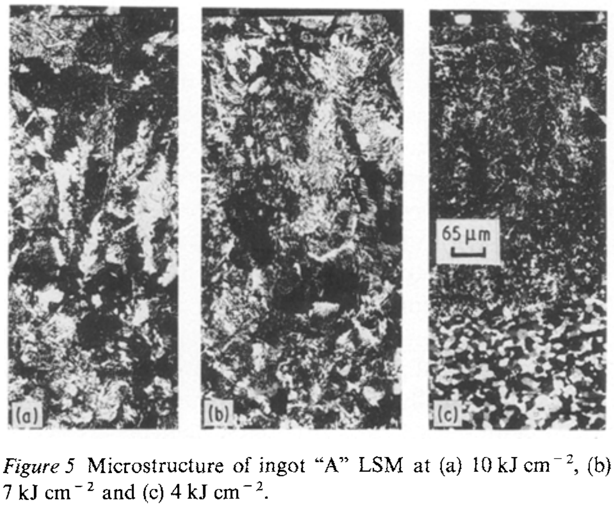

Figure 5 Microstructure of ingot "A" LSM at (a) 10 kJ cm^{-2}, (b) 7 kJ cm^{-2} and (c) 4 kJ cm^{-2}.

Melt-pool depth is directly related to applied energy density. The lowest laser energy density (4 kJ cm^{-2}) consistently produced the shallowest melt pool, whereas 7 and 10 kJ cm^{-2} laser energy densities produced about the same melt pool depths. Table VI lists melt-pool depths for each processed group.

The highest laser energy density (10 kJ cm^{-2}) generated the coarsest microstructure. When examining the topmost surface region, wider spacing of the parallel platelets within each grain is discernible. Larger colony sizes are associated with the topmost layer than with the melt-pool periphery. Both of these attributes are characteristic of slower quench rates.

Medium energy density (7 kJ cm^{-2}) shows medium refinement of microstructure when compared to the lowest and highest energy densities. Medium energy density produced material with the greatest amount of Widmanstatten (basketweave) structure and colonies of medium size with parallel platelet spacing of medium dimensions.

Analysing for possible chemical segregation in LSM samples is difficult, due to the inherently low alloy content within these materials. Zr-4 material has the highest alloy content consisting of 15000 p.p.m. Sn, 2000 p.p.m. Fe, and 1000 p.p.m. Cr. Pure zirconium contains 100 p.p.m. Sn, 600 p.p.m. Fe, and 100 p.p.m. Cr. Segregation effects consist of enriched areas and partially depleted zones of two to ten times the bulk concentration. It is difficult, if not impossible, for SEM–EDX and electron microprobe to locate segregated areas and quantify enriched or partially depleted zones due to the large volume of material excited by the probing beam.

Optical microscopy is capable of distinguishing the melt-pool periphery using an etch developed specifically for highlighting tin-rich areas [21]. The melt-pool periphery is highlighted and resembles an arc initiating at the surface, extending to the bottom of the melt pool and intersecting the subsequent melt pool.

SIMS, with a resolution level of approximately 2 µm, was employed to study microsegregation by analysing a 2 µm diameter by ten atom layers deep volume [22]. Tin and iron were found to be segregated. Tin is more concentrated at the melt-pool wall, where it is twice as high as in the central region of the melt pool (see Fig. 6 and Table VII). Tin-rich arcs

TABLE VI Melt-pool depths (mm)

Energy	Pure Zr		Zr-4	Zr 702		Average
(kJ cm^{-2})	A	B	G	D^{a}	E	n = 4
4	0.46	0.53	0.53	0.51	0.38	0.47
7	0.99	1.04	1.09	0.91	1.07	1.05
10	1.19	1.07	1.24	1.90	1.10	1.15

^{a}Sample thickness 2.0 mm, all other samples were 3.4 mm; these values were excluded from averages.

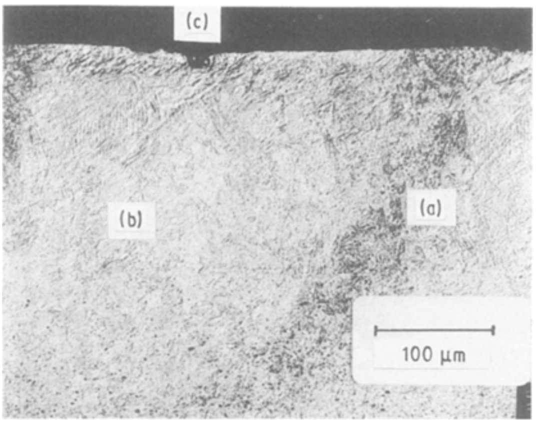

Figure 6 Tin and iron segregation within the melt pool: (a) tin-rich arc, (b) iron-rich arc parallel with tin-rich arc, (c) corrosion initiation site.

TABLE VII Tin and iron segregation (p.p.m.) in ingots A, D and G

Element/position	pure Zr, A	Zr-702, D	Zr-4, G
Tin			
matrix	500	1900	14 800
melt-pool edge	1000	3500	28 000
Iron			
matrix	600	850	2 080
melt-pool	5500	8000	20 000

extend from the surface, down to the bottom of the pool, and then intersect the adjacent melt-pool periphery (overlapping of laser beam passes).

Iron-rich areas were located in the melt-pool approximately 200 µm from the melt-pool wall. These iron-rich arcs are parallel to the tin-rich arcs, but are higher in iron than the melt pool by a factor of ten, and coincide with the nodule genesis location. The tin-rich arcs are iron-poor, whereas the iron-rich arcs have a concentration level of tin similar to the melt pool.

4. Discussion

Microstructure is refined by LSM. Wrought product (non-LSM) exhibited an equiaxed coarse-grained structure. The lowest laser energy density (4 kJ cm^{-2}) produces the fastest quench, and the finest microstructure, resulting from the small melt pool and the large heat reservoir. By comparison the highest laser energy density (10 kJ cm^{-2}) produced a slower quench rate and a correspondingly slightly coarser microstructure, that was, however, much finer than the wrought product microstructure.

The variation in microstructure affected the corrosion performance during corrosion testing. The overall corrosion performance of the LSM coupons tested in the steam autoclave was poor. Laser processing greatly reduces the corrosion resistance. Nodular corrosion is accelerated in the laser pass overlap region and the location of the nodular corrosion product on the laser passes coincides with the location of the iron-rich areas within the melt zone. These localized iron-rich areas are responsible for the accelerated corrosion.

The immersion tests, conducted in a 10% $FeCl_3$ environment, showed that the fastest LSM quench generated the finest microstructure, resulting in improved corrosion resistance. Up to a 600-fold increase in corrosion resistance was achieved and the propensity for pitting was significantly reduced. The slower quench, from the highest laser energy density (10 kJ cm^{-2}), yielded a corrosion resistance less than the fastest quench, but still an order of magnitude better than that of the wrought product (the slowest quench rate).

Pitting corrosion that results from immersion in $FeCl_3$ solution is periodic, similar to the appearance of the nodular corrosion appearing predominantly in the laser pass overlap region.

The martensitic type microstructure provides the best corrosion resistance in an acid environment, while the coarser, wrought product microstructure performs the best in a steam autoclave environment. This is due to the different type of corrosion that occurs in each environment.

In the steam environment, zirconium behaves anodically, combining with the available oxygen, producing an oxide film [32]. The second-phase particles [Zr(Fe,Cr) precipitates] behave cathodically, completing the required electron circuitry. As long as the electrical circuit is maintained, a tightly adherent, slow growing, protective oxide film is generated [34]. When the oxide film exceeds several micrometres in thickness it loses its protective behaviour and degrades, permitting accelerated oxidation. Because the iron is concentrated in specific locations within each melt pool, the electrochemical behaviour is enhanced in these isolated areas. The higher concentration of iron increases the local oxidation rate.

Solute transport is considered to occur only in the liquid phase, while energy transport is considered in both liquid and solid phases [23, 24]. During solidification of the liquid, alloy elements and impurities are attracted to the liquid–gas surface if they have an affinity for higher temperature phases [35]. As the liquid–solid interface moves towards the liquid–gas surface, atoms rejected from the freezing solid enter the liquid and are redistributed by diffusion and turbulent mixing [28].

Laser processing causes tin and iron segregation. The tin-rich areas result from solidification kinetics in the zirconium-based alloys. The tin segregates to the portion of the melt that solidifies first, because tin prefers the lower temperature phase of zirconium (alpha). The iron remains in solution for a longer period of time because it prefers the high temperature phase of zirconium (beta).

In an acid environment, zirconium atoms behave cathodically and alloying elements, iron in particular, behave anodically [36]. As in the autoclave environment, both the iron and zirconium elements are necessary for corrosion to occur. In the acid environment, the chemical reaction results in the zirconium ionizing, disassociating from the matrix, and migrating into the acid solution. Because the iron-rich areas are localized in the laser pass overlap region, the pitting occurs preferentially in these areas [37]. The iron-rich areas promote the dissolution of zirconium ions from the matrix, resulting in the formation of a pit. The lower iron concentration everywhere else in the LSM surface provides a pit-resistant surface and reduces the general corrosion rate.

5. Conclusions

As the laser energy density decreases, the melt-pool depth decreases, the quench rate increases, and the microstructure becomes increasingly refined as shown by the interlamellar spacing within each grain.

LSM results in iron and tin segregation. The corrosion tests simulated the typical environments, to which zirconium-based alloys are subjected. Nodular corrosion initiates at the laser pass overlap regions due to iron segregation, which causes accelerated oxidation due to increased ion concentration in localized areas. As the laser energy density and beam width decrease, the number of laser pass overlap regions increases, and the corrosion resistance decreases. This is directly related to the increased surface area that contains the iron-rich segregation.

As the quench rate increases due to LSM, the transition point (time to transition and corrosion rate at transition) increases.

LSM increases the corrosion resistance in 10% $FeCl_3$ due to the second-phase particles dissolving and remaining in the melt as a supersaturated solid solution.

Laser processing reduces the propensity for pitting.

Acknowledgements

This research was funded by an educational grant by the Babcock & Wilcox Co. to Wayne Reitz.

References

1. M. G. FONTANA, in "Advances in Corrosion Science and Technology", Vol. 6, edited by M. G. Fontana and R. W. Staehle (Plenum, New York, 1976) pp. 227–45.
2. H. G. RICKOVER, L. D. GIEGER, and B. LUSTMAN, NR: D; 1975, USERDA, March 1975, p. 1081.
3. J. N. WANKLYN and P. J. JONES, *J. Nucl. Mater.* **6** (1962) 291.
4. V. QUACH and D. O. NORTHWOOD, "Optimizing Materials for Nuclear Application" (1984) pp. 51–62.
5. A. B. JOHNSON Jr, ASTM STP 458 (American Society for Testing and Materials, Philadelphia, 1969) pp. 271–85.
6. S. KASS, ASTM STP 368 (American Society for Testing and Materials, Philadelphia, 1964) pp. 3–27.
7. J. N. WANKLYN, ASTM STP 368 (American Society for Testing and Materials, Philadelphia, 1964) pp. 58–75.
8. B. COX, in "Advances in Corrosion Science and Technology", Vol. 5, edited by M. G. Fontana and R. W. Staehle (Plenum, New York, 1976) pp. 251–321.
9. M. A. MAGUIRE and T. L. YAU, NACE Conference, Paper No. 265 (1986) pp. 1–20.
10. J. H. SCHEMEL, ASTM STP 639 (American Society for Testing and Materials, Philadelphia, 1977) pp. 1–93.
11. T. L. YAU and M. A. MAGUIRE, *Corrosion* **40** (1984) 289.
12. *Idem, ibid.* **41** (1985) 397.
13. R. W. OHSE, *Pure Appl. Chem.*, **60** (1988) 309.
14. Y. ARATA, "Plasma, Electron and Laser Beam Technology," (ASM, Metals Park, OH, 1986).
15. C. W. DRAPER, F. J. den BROEDER, D. C. JACOBSON, E. N. KAUFMANN, M. L. McDONALD and J. M. VANDENBERG, "Laser and Electron-Beam Interactions with Solids" (Elsevier Science, 1982) pp. 419–424.
16. E. McCAFFERTY and P. G. MOORE, "Laser Surface Treatment of Metals", edited by C. W. Draper and P. Mazzoldi (Martinus Nijhoff, Boston, 1986) pp. 263–95.
17. J. W. DAVIS, A. A. HAASZ and P. C. STANGEBY, *J. Nucl. Mater.* **138** (1986) 227.
18. W. M. STEEN, "International Conference on Advances in Surface Coating Technology" (The Welding Institute, Avington, Cambridge, 1978) pp. 175–87.
19. C. R. CLAYTON, "Environmental Degradation of Ion and Laser Beam Treated Surfaces", edited by G. S. Wart and K. S. Grabowski (TMS, Philadelphia, 1989) pp. 33–55.
20. J. M. POATE, *ibid.* pp. 23–30.
21. W. REITZ and J. RAWERS, *J. Mater. Sci. Lett.* **9** (1990) 1365.
22. C. EVANS Jr and R. BLATTNER, *Newsletter, Charles Evans and Assoc.* **5** (2) (1990) pp. 10–11.
23. M. J. AZIZ, *J. Appl. Phys.* **53** (1982) 1158.
24. A. KAR and J. MAZUMDER, *ibid.* **61** (1987) 2645.
25. J. MAZUMDER and W. M. STEEN, in "Laser '77", Opto-Electronics Conference, edited by W. Weidelich (1977) pp. 304–15.
26. *Idem, Metal Construct.* **12** (1980) 423.
27. T. CHANDE and J. MAZUMDER, *Met. Trans.* **14B** (1983) 181.
28. P. BAERI, S. U. COMPISANO, M. G. GRIMALDI and E. RIMINI, in "Laser and Electron Beam Processing of Materials", MRS Symposium (1979) pp. 130–6.
29. C. W. DRAPER, *ibid.* pp. 721–7.
30. A. RICHARD, "*Fr. Ann. Chem.* **13** (1988) 284.
31. E. HILLNER, ASTM STP 633, (American Society for Testing and Materials, Philadelphia, 1977) pp. 211–35.
32. T. L. YAU, "Corrosion and Corrosion Protection Handbook", edited by P.A. Schweitzer (Marcel Dekker, New York, 1988) pp. 231–78.
33. R. KUWAE, K. SATO, J. KAWASHIMA and E. HIGASHINAKAGAWA, *N. Nucl. Sci. Tech.* **23** (1986) 661.
34. N. SATO, *Corrosion* **45** (1989) 354.
35. D. M. FOLLSTAEDT, in "Laser and Electron-Beam Interactions with Solids", MRS Symposium (1981) pp. 377–87.
36. M. J. CHAPPEL and J. S. LEACH, "*Passivity of Metals*" (Electrochemical Society, Houston, Texas, 1978) pp. 1003–34.
37. S. SMITH, *Charles Evans and Assoc. Report* 13 May (1990) 1.

Received 15 January
and accepted 7 June 1991